

Hydrogenated Amorphous Silicon Carbide: A Low-Loss Deposited Dielectric for Microwave to Submillimeter-Wave Superconducting Circuits

B.T. Buijtendorp^{1,*}, S. Vollebregt¹, K. Karatsu^{1,2}, D.J. Thoen¹, V. Murugesan,²
K. Kouwenhoven^{1,2}, S. Hähnle^{1,2}, J.J.A. Baselmans,^{1,2} and A. Endo¹

¹*Faculty of Electrical Engineering, Mathematics and Computer Science, Delft University of Technology,
Mekelweg 4, Delft 2628 CD, Netherlands*

²*SRON Netherlands Institute for Space Research, Niels Bohrweg 4, Leiden 2333 CA, Netherlands*

(Received 8 October 2021; revised 21 September 2022; accepted 7 November 2022; published 1 December 2022)

Low-loss deposited dielectrics will benefit superconducting devices such as integrated superconducting spectrometers, superconducting qubits, and kinetic inductance parametric amplifiers. Compared with planar structures, multilayer structures such as microstrips are more compact and eliminate radiation loss at high frequencies. Multilayer structures are most easily fabricated with deposited dielectrics, which typically exhibit higher dielectric loss than crystalline dielectrics. We measure the subkelvin and low-power microwave and millimeter-submillimeter-wave dielectric loss of hydrogenated amorphous silicon carbide (α -SiC:H), using superconducting chips with Nb-Ti-N/ α -SiC:H/Nb-Ti-N microstrip resonators. We deposit the α -SiC:H by plasma-enhanced chemical vapor deposition at a substrate temperature of 400 °C. The α -SiC:H has a millimeter-submillimeter loss tangent ranging from 0.9×10^{-4} at 270 GHz to 1.5×10^{-4} at 385 GHz. The microwave loss tangent is 3.1×10^{-5} . These are the lowest low-power subkelvin loss tangents that have been reported for microstrip resonators at millimeter-submillimeter and microwave frequencies. The α -SiC:H films are free of blisters and have low stress: –20 MPa compressive at 200-nm thickness to 60 MPa tensile at 1000-nm thickness.

DOI: 10.1103/PhysRevApplied.18.064003

I. INTRODUCTION

Superconducting transmission lines are essential components of devices such as integrated superconducting spectrometers (ISSs) [1–3], kinetic inductance parametric amplifiers (KIPAs) [4], and superconducting qubits [5]. These superconducting devices operate at subkelvin temperatures where amorphous solids exhibit excess dielectric loss compared with their crystalline counterparts [6,7]. This is problematic since such loss limits the efficiency and spectral resolution of ISSs [8], decreases the gain of KIPAs [9,10], and is a significant source of decoherence in superconducting qubits [11]. The problem is often circumvented by avoiding deposited dielectrics, for example by employing planar structures. However, a low-loss deposited dielectric will enable the use of multilayer structures such as microstrips and parallel plate capacitors, thereby achieving benefits such as miniaturization [10,12,13] and the removal of radiation loss [14].

Microstrip resonators with hydrogenated amorphous silicon (α -Si:H) deposited by plasma-enhanced chemical vapor deposition (PECVD) exhibit very low subkelvin and low-power dielectric loss tangents $\tan \delta$ of $(4\text{--}5) \times 10^{-5}$ at

microwave frequencies [12,15–17] and $2.1 \pm 0.1 \times 10^{-4}$ at 350 GHz [16]. Although this is an improvement over SiO_2 [15,18] and SiN_x [8,15,19], a further reduction in $\tan \delta$ is desirable. For example, a smaller $\tan \delta$ enables a proportionally larger resolving power $R = f/\Delta f$ for the millimeter-submillimeter (mm-submm) filters of an ISS, without sacrificing filter efficiency [8].

The dielectric loss in superconducting microwave resonators is successfully modeled as absorption by two-level systems (TLSs) [6,7,15,20]. Although the microscopic origin of the TLSs remains unknown [6,7], a comparison of SiO_2 , SiN_x , α -Si:H, and crystalline Si (c -Si) has led to the hypothesis that a more constrained lattice (i.e., an increase in coordination number) is correlated with a decrease in dielectric loss [15]. With electron-beam-evaporated α -Si it has been observed that a lower microwave loss can be achieved by depositing at elevated substrate temperatures (T_{sub}), and a correlation was found between the microwave loss and the dangling bond density [21]. Electron-beam-evaporated and sputtered α -Si films, which are hydrogen-free, exhibit an order of magnitude larger microwave loss than α -Si:H [15,21], suggesting that there is a relation between nonpassivated dangling bonds and dielectric loss.

Hydrogenated amorphous silicon carbide (α -SiC:H) is a fourfold-coordinated and hydrogenated material, similar

*b.t.buijtendorp@tudelft.nl

to a -Si:H. Low-stress a -SiC:H films can be deposited by PECVD at high T_{sub} [22]. The material properties of a -SiC:H such as the dielectric constant ϵ_r , hydrogen content, residual stress, band gap, and silicon-to-carbon ratio can to a large degree be tuned by varying the deposition conditions [22,23]. The a -SiC:H films do not exhibit blisters, which are a common issue with a -Si:H [24,25]. Furthermore, a -SiC:H has high wet etching selectivity with Si [22], enabling an a -SiC:H film to be used as a membrane, for example in superconducting photon detectors [26]. These properties suggest that a -SiC:H is a promising alternative to a -Si:H and SiN_x for superconducting devices. However, the subkelvin and low-power microwave and mm-submm-wave dielectric losses of a -SiC:H have not yet been reported. Here we present measurements of the subkelvin and low-power dielectric loss of a -SiC:H at microwave (7 GHz) and mm-submm (270–385 GHz) frequencies.

II. DEVICE FABRICATION

The losses are measured on superconducting chips with Nb-Ti-N/ a -SiC:H/Nb-Ti-N microstrip resonators, with an identical design for each chip. Figure 1(a) shows a photograph of one of the chips. The fabrication details for an equivalent chip with a -Si:H instead of a -SiC:H have previously been reported [16]. The Nb-Ti-N films are sputter-deposited using a Nordiko 2000 [27]. The Nb-Ti-N ground plane under the a -SiC:H is 135-nm thick and the Nb-Ti-N line on top of the a -SiC:H is 150-nm thick, measured using step profilometry and tilted scanning electron microscopy at the position of the Fabry-Perot resonators [FP1–4 in Fig. 1(a)].

A 295-nm-thick a -SiC:H film is deposited by PECVD using a Novellus Concept One [22,28]. The precursor gases are silane (SiH_4) and methane (CH_4) with flow rates of 25 and 411 sccm, respectively, and no dilution gas. We deposit the a -SiC:H with a T_{sub} of 400 °C, chamber pressure of 2 Torr, 450-kHz rf power of 150 W, and 13.56-MHz rf power of 450 W. We pattern the a -SiC:H layer using reactive ion etching with an SF_6 and O_2 plasma at a rate of approximately 0.8 nm/s.

III. DIELECTRIC LOSS MEASUREMENTS

A. Method for mm-submm loss measurements

The loss measurement device and experimental setup are equivalent to what has been reported for earlier work on a -Si:H [16]. We measure the mm-submm loss at 120 mK by analyzing the transmission through four in-line Nb-Ti-N/ a -SiC:H/Nb-Ti-N microstrip FPs (FP1–4) with 2- μm line width. Each FP is coupled to a Nb-Ti-N coplanar waveguide (CPW) feed line on one end and to a hybrid Nb-Ti-N-Al microwave kinetic inductance detector (MKID) on the other end.

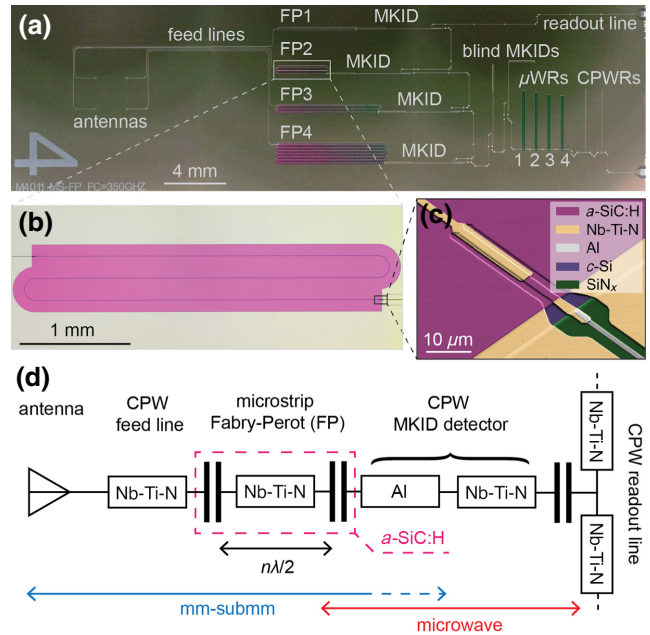


FIG. 1. (a) Photograph of chip 2. The four Fabry-Perot resonators (FP1–4) receive the mm-submm signal from antennas that receive radiation from a Toptica TeraBeam 1550 photomixer source. Each FP is coupled to a MKID. The four shunted microstrip microwave resonators ($\mu\text{WR}1$ –4) are coupled to the readout line. (b) Micrograph of FP2. The purple area is a -SiC:H. The feed line is visible on the left of the image and the MKID is visible on the right. (c) Tilted scanning electron micrograph of the coupling of FP2 to the MKID, with false coloring. (d) Schematic of an antenna-FP-MKID circuit. The FPs have a length of an integer (mode number n) multiple of half the mm-submm wavelength λ , and have transmission peaks at nf_0 , where f_0 is the fundamental resonance frequency. The mm-submm signal is absorbed in the Al section of the MKID, resulting in a change of resonance frequency (frequency response) of the MKID.

[29] on the other end, as shown for FP2 in the micrograph in Fig. 1(b). The FPs' couplers all have an identical design. Figure 1(c) shows a scanning electron micrograph of the coupling of FP2 to a MKID. Each feed line is connected to a twin slot antenna with a center frequency of 350 GHz, which is located in the focus of a Si lens glued to the backside of the chip. The antennas receive mm-submm radiation from a Toptica Photonics TeraBeam 1550 continuous-wave photomixer source. The MKIDs are coupled to a shared Nb-Ti-N CPW microwave readout line, which we read out using a frequency-multiplexed readout system [30].

A schematic of the mm-submm experiment is given in Fig. 1(d). The different lengths of the FPs result in different fundamental resonance frequencies f_0 . The FPs have transmission peaks at integer multiples (mode numbers n) of f_0 . The power that is transmitted through a FP breaks Cooper pairs in the Al section of the MKID, resulting in a change

in the MKID's resonance frequency (frequency response) [31]. The frequency response is corrected for stray light by dividing by the response of a MKID that is not connected to a FP [blind MKID in Fig. 1(a)].

Since the MKIDs' frequency responses are linear in power [32], they trace the $|S_{21}(f)|^2$ transmission curves of the FPs. The transmission of the mm-submm power through a FP is a sum of Lorentzian peaks [33] and therefore we can obtain the FP's loaded quality factor Q from the transmission peaks as $Q = f_{\text{peak}}/\Delta f$, where f_{peak} is the peak's center frequency and Δf is the peak's full width at half maximum.

The frequency response is measured from 250 to 400 GHz by sweeping the photomixer source in steps of 20 MHz. We separate the frequency response data into four bands centered around 270, 310, 350, and 385 GHz to determine the loss of the $a\text{-SiC:H}$ at these four frequencies. The frequency bands are shown by the vertical dashed lines in Fig. 4.

In each band and for each FP we obtain the average n and the average Q , from which we obtain the internal quality factors Q_i by fitting to the following equation [16]:

$$Q = \frac{nQ_{c,1}Q_i}{nQ_{c,1} + Q_i}, \quad (1)$$

where $Q_c = nQ_{c,1}$ is the FP's coupling quality factor. Here $Q_{c,1} = \pi/|t_c|^2$, with t_c the coupler's transmission coefficient. The $\tan \delta$ is obtained from Q_i as

$$\tan \delta = 1/(pQ_i), \quad (2)$$

where p is the filling fraction [20] of the dielectric, which we determine to be 0.97 in our microstrip resonators using the electromagnetic-field solver Sonnet [34].

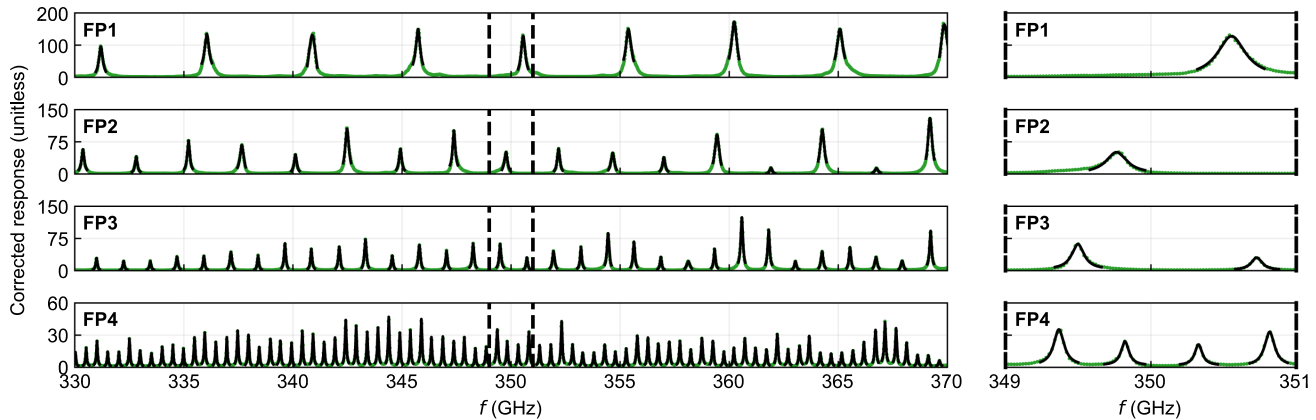


FIG. 2. The measured frequency response in the 330–370-GHz band for chip 1. The response is measured by the MKIDs that are coupled to FP1–4. The response is corrected for stray light by dividing by the response of a MKID that is not coupled to a FP [blind MKID in Fig. 1(a)]. The green dots represent the measured response, and the black curves are Lorentzian fits to the peaks, from which we obtain the average Q for each FP. The same analysis is performed for each of the four frequency bands. The right-hand plot shows the same data enlarged for 349–351 GHz.

B. Mm-submm loss results and discussion

We measure the mm-submm loss of the $a\text{-SiC:H}$ on two chips (chips 1 and 2) fabricated on the same wafer. To illustrate the response, we give in Fig. 2 the response in the 330–370-GHz band of the four MKIDs behind the four FPs of chip 1. The measured Q versus n and the fits to Eq. (1) of chip 1 are shown in Fig. 3. An equivalent plot for chip 2 is shown in Appendix A. In the fits of Eq. (1) the standard errors in the average Q are used as fitting weights. In addition to obtaining the Q_i values, from this fit we also obtain the $Q_{c,1}$ values of chips 1 and 2. The measured $Q_{c,1}$ values are given in Appendix A.

The resulting $\tan \delta$ values of chips 1 and 2 are plotted in Fig. 4. The mm-submm $\tan \delta$ of the $a\text{-SiC:H}$ ranges from 0.9×10^{-4} at 270 GHz to 1.5×10^{-4} at 385 GHz, averaged over chips 1 and 2. These losses are significantly lower than what has been reported for other dielectrics such as $a\text{-Si:H}$ [16] and SiN_x [8,19]. At 350 GHz the $a\text{-SiC:H}$ exhibits a $\tan \delta$ of 1.3×10^{-4} , compared with a $\tan \delta$ of 2.1×10^{-4} for $a\text{-Si:H}$, which was measured using the same experimental method [16].

We calculate that the internal mm-submm power $P_{\text{int,FP}}$ circulating inside the FPs is below 1 pW, corresponding to an average number of photons per half-wavelength $N < 1$. We do not observe a significant correlation between $P_{\text{int,FP}}$ and the loss tangent $\tan \delta$ of the $a\text{-SiC:H}$, suggesting that TLS saturation [6,20] does not affect the mm-submm loss measurements. More information on this calculation is given in the Supplemental Material [35].

C. Method for microwave loss measurements

We measure the microwave loss of the $a\text{-SiC:H}$ on two chips (chips 1 and 3) fabricated on the same wafer,

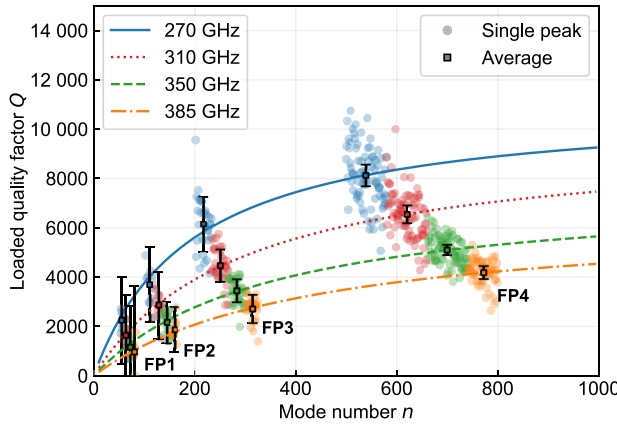


FIG. 3. Loaded quality factor Q versus mode number n of FP1–4 of chip 1. The curves are fits of Eq. (1) to the average Q and average n values. The error bars represent 30 standard errors (± 30 SE) in Q and the $1/\text{SE}$ values are used as fitting weights.

where chip 1 is the same chip as discussed for the mm-submm loss measurements. On each chip, the microwave losses are measured using four Nb-Ti-N/ a -SiC:H/Nb-Ti-N half-wavelength microstrip microwave resonators [$\mu\text{WR}1$ –4 in Fig. 1(a)] with 2- μm line width, at a temperature of 60 mK. We use a vector network analyzer to measure the S_{21} parameter of the Nb-Ti-N CPW readout line, which is coupled to the four shunted μWRs . We measure $\tan \delta$ in a range of microwave internal resonator powers P_{int} , corresponding to an average number of photons per half-wavelength in the resonators N of roughly 10^{-1} – 10^8 . N is equal to $N = P_{\text{int}} / (\hbar f^2)$. We fit the $|S_{21}|$ dips of the four μWRs using the model described in Ref. [36] to obtain the resonators' Q_i , from which we calculate $\tan \delta$ [Eq. (2)].

D. Microwave loss results and discussion

From Fig. 5 we observe that the microwave $\tan \delta$ follows the power dependence predicted by the standard tunneling model (STM) [6,20]:

$$\tan \delta = \tan \delta_0 \tanh \frac{\hbar f}{2k_B T} \left(1 + \frac{N}{N_0} \right)^{-\beta/2} + \tan \delta_{\text{HP}}, \quad (3)$$

where f is the frequency, T is the temperature, N_0 is the critical photon number above which the TLSs saturate, and β is equal to 1 in the STM, but it has previously been observed in the range of 0.3–0.7 [7,16,21]. The $\tan \delta_{\text{HP}}$ term represents losses other than TLS loss that dominate at high internal resonator power. The $\tan \delta_0$ is the TLS-induced $\tan \delta$ in the low-power limit and at 0 K.

We obtain the microwave $\tan \delta_0$ and β by fitting Eq. (3) to the measured $\tan \delta$ versus N . The fits for chip 1 are shown in Fig. 5 and the fits for chip 3 are shown in Appendix B. The μWRs of chips 1 and 3 exhibit an average $\tan \delta_0$ of $(3.1 \pm 0.4) \times 10^{-5}$. This is comparable to

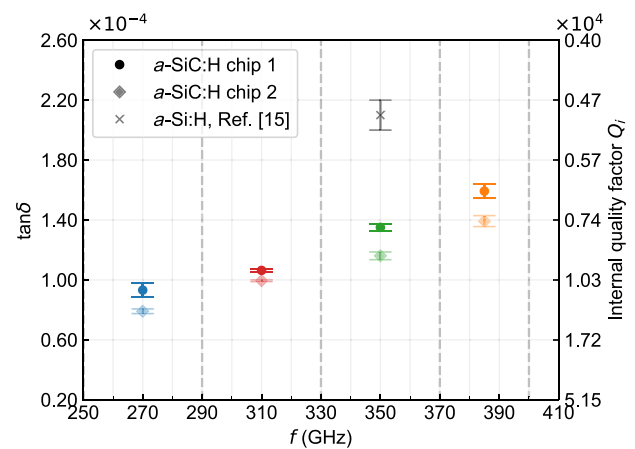


FIG. 4. The mm-submm $\tan \delta = 1/(pQ_i)$ versus frequency for chips 1 and 2. The error bars represent one standard deviation ($\pm \sigma$). The frequency bands over which Q and n are averaged are displayed by the vertical dashed lines. The a -Si:H loss value at 350 GHz was reported in earlier work and was measured using the same experimental method [16].

what has been reported for a -Si:H [12,15,16]. We measure β values in the range of 0.5–0.8. We confirm that the low-power loss is dominated by the a -SiC:H and not by the Nb-Ti-N by measuring a shunted Nb-Ti-N CPW quarter-wavelength microwave resonator (CPWR) with a 6- μm center line width and a 16- μm gap width, which is fabricated directly on top of the c -Si substrate ($\rho > 10 \text{ k}\Omega \text{ cm}$), i.e., without a -SiC:H. The low-power $1/Q_i$ of $(4.1 \pm 0.1) \times 10^{-6}$ of the CPWR is significantly smaller than that of the μWRs .

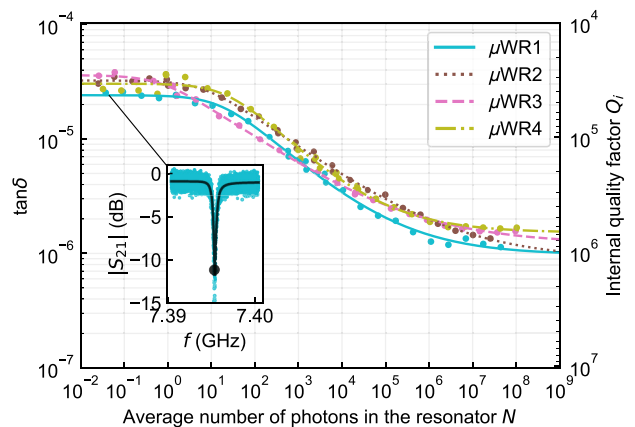


FIG. 5. Measured microwave $\tan \delta = 1/(pQ_i)$ versus average number of photons in the resonators $\mu\text{WR}1$ –4 of chip 1. The curves are fits to Eq. (3). The inset illustrates how $\tan \delta$ is obtained at each power, by fitting the $|S_{21}|$ dips using the model in Ref. [36]. The $\tan \delta_0$ values are obtained by fitting the $\tan \delta$ versus N curves to Eq. (3).

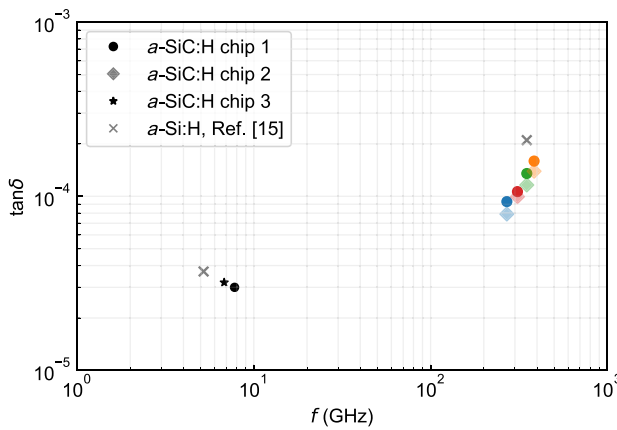


FIG. 6. Overview of the mm-submm $\tan \delta = 1/(pQ_i)$ values of chips 1 and 2, together with the microwave $\tan \delta_0$ values of chips 1 and 3. The $\tan \delta_0$ values are obtained from Eq. (3). The $a\text{-Si:H}$ loss value at 350 GHz was reported in earlier work and was measured using the same experimental method [16].

E. Discussion on the physical origin of the loss

The physical origin of the loss is not yet fully understood. We give an overview of the measured losses in Fig. 6, together with data from Ref. [16] for $a\text{-Si:H}$. The microwave loss of the $a\text{-SiC:H}$ is well described by the STM for TLSs. However, the significantly larger mm-submm loss than microwave loss as well as the frequency dependence of the mm-submm loss are surprising in the framework of the STM, which assumes a frequency-independent TLS density of states [6]. We note that a larger mm-submm than microwave loss was also reported for SiN_x [15,19] and $a\text{-Si:H}$ [15,16]. Although a generalized TLS model with a frequency-dependent TLS density of states has been reported [37], from Fig. 6 we observe that the mm-submm loss follows a power-law dependence that does not extrapolate to the microwave loss value. This leads us to the hypothesis that the mm-submm loss has an origin different from that of the microwave loss. We suggest that the microwave loss of the $a\text{-SiC:H}$ is dominated by TLS loss, whereas the mm-submm loss is dominated by the absorption tail of phonon modes at far-infrared wavelengths [16,38,39].

IV. DIELECTRIC CONSTANT, FILM UNIFORMITY, AND RESIDUAL STRESS

We estimate the subkelvin dielectric constant ε_r of the $a\text{-SiC:H}$ by comparing the measured resonance frequencies of $\mu\text{WR1-4}$ and FP1-4 with Sonnet [34] simulations of the microstrips. We find an ε_r of 7.8 ± 0.7 , where the uncertainty is due to the nonuniformity and uncertainty in the Nb-Ti-N properties across the wafer [27]. Within this uncertainty the microwave and mm-submm ε_r are indistinguishable.

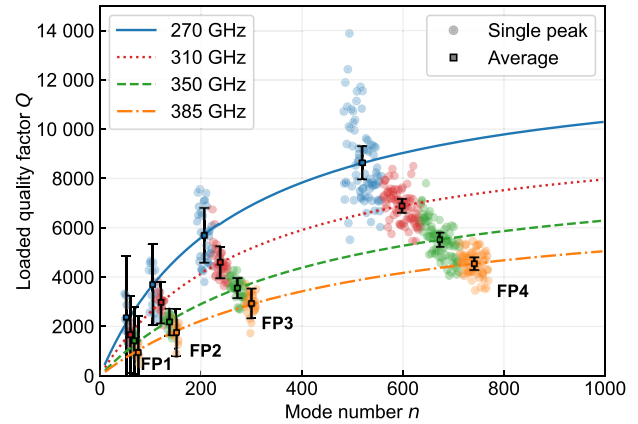


FIG. 7. Loaded quality factor Q versus mode number n of FP1–4 of chip 2. The curves are fits of Eq. (1) to the average Q and average n values. The error bars represent 30 standard errors ($\pm 30 \text{ SE}$) in Q and the $1/\text{SE}$ values are used as fitting weights.

We use ellipsometry to measure a room-temperature ε_r of 7.5 at 250 THz (1200 nm) at the wafer's center, with a nonuniformity in $\varepsilon_r < 1\%$ within a 3.5-cm radius around the wafer's center. Furthermore, from the ellipsometry measurement we determine the film thickness to be 295 nm at the wafer's center, with a nonuniformity in thickness $< 1\%$. The excellent uniformity in thickness and dielectric constant suggests that the deposition process of the $a\text{-SiC:H}$ is highly uniform across the wafer. From the same ellipsometry measurement, we observe a band gap of 1.8 eV, which we obtain by fitting the Tauc-Lorentz dispersion model to the ellipsometry data in the range of 0.8–2.7 eV.

We determine the residual stress of the $a\text{-SiC:H}$ films from the wafer bow before and after deposition on bare $c\text{-Si}$ substrates, using the Stoney equation. The wafer bow is measured using a Flexus 2320-S. The $a\text{-SiC:H}$ films exhibit low stress: –20 MPa compressive at 200-nm thickness to 60 MPa tensile at 1000-nm thickness.

V. CONCLUSION

To conclude, PECVD $a\text{-SiC:H}$ exhibits the lowest low-power subkelvin mm-submm dielectric loss that has been reported to date for microstrip resonators. The microwave loss is comparable to the best values that have been reported for microstrip resonators [12,16]. In addition to the low loss, the $a\text{-SiC:H}$ films are free of blisters, exhibit low stress, and have excellent uniformity in terms of the thickness and dielectric constant measured by ellipsometry. These properties make $a\text{-SiC:H}$ a promising dielectric for microwave to submm-wave superconducting circuits in many applications.

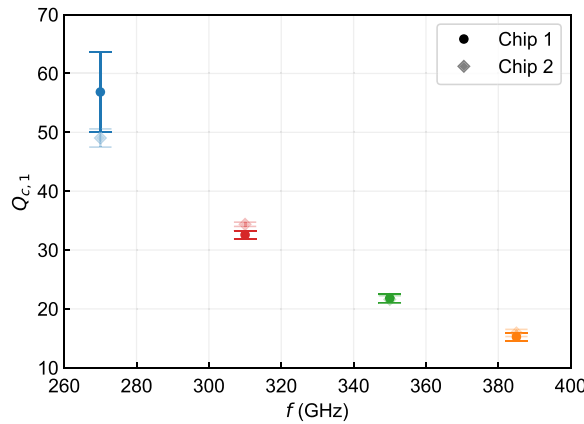


FIG. 8. The FP coupler's $Q_{c,1}$ versus frequency for chips 1 and 2, obtained from the fit of the Q versus n data to Eq. (1). The error bars represent one standard deviation ($\pm\sigma$).

ACKNOWLEDGMENTS

We thank the staff of the Else Kooi Laboratory and the Kavli Nanolab Delft for their support. This work is supported by the European Union (ERC Consolidator Grant No. 101043486 TIFUUN). Views and opinions expressed are however those of the authors only and do not necessarily reflect those of the European Union or the European Research Council Executive Agency. Neither the European Union nor the granting authority can be held responsible for them.

APPENDIX A: ADDITIONAL MM-SUBMM LOSS DATA

In Fig. 7 we show the mm-submm Q versus n data of chip 2, which is fabricated on the same wafer as chip 1. In

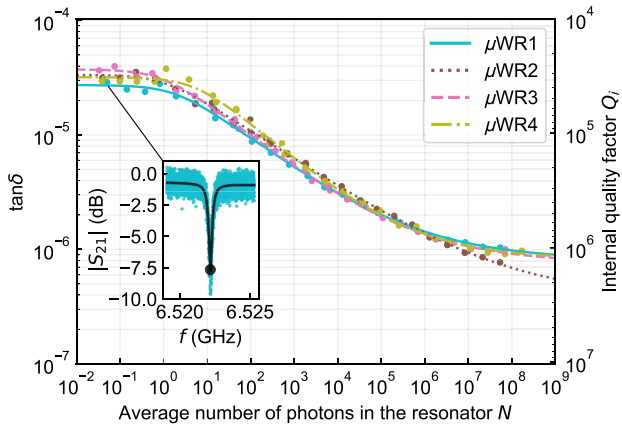


FIG. 9. Measured microwave $\tan \delta = 1/(pQ_i)$ versus average number of photons in the resonators $\mu\text{WR}1\text{--}4$ of chip 3. The curves are fits to Eq. (3). The inset illustrates how $\tan \delta$ is obtained at each power, by fitting the $|S_{21}|$ dips using the model in Ref. [36]. The $\tan \delta_0$ values are obtained by fitting the $\tan \delta$ versus N curves to Eq. (3).

Fig. 8 we plot the $Q_{c,1}$ values of chips 1 and 2, which we obtain from the fits to Eq. (1).

APPENDIX B: ADDITIONAL MICROWAVE LOSS DATA

In Fig. 9 we plot the microwave $\tan \delta$ versus N data of chip 3, which is fabricated on the same wafer as chip 1.

- [1] A. Endo *et al.*, First light demonstration of the integrated superconducting spectrometer, *Nat. Astron.* **3**, 989 (2019).
- [2] K. S. Karkare, P. S. Barry, C. M. Bradford, S. Chapman, S. Doyle, J. Glenn, S. Gordon, S. Hailey-Dunsheath, R. M. Janssen, A. Kovács, H. G. LeDuc, P. Mauskopf, R. McGeehan, J. Redford, E. Shirokoff, C. Tucker, J. Wheeler, and J. Zmuidzinas, Full-array noise performance of deployment-grade superspec mm-wave on-chip spectrometers, *J. Low Temp. Phys.* **199**, 849 (2020).
- [3] A. Endo, K. Karatsu, A. P. Laguna, B. Mirzaei, R. Huiting, D. J. Thoen, V. Murugesan, S. J. C. Yates, J. Bueno, N. v. Marrewijk, S. Bosma, O. Yurduseven, N. Llombart, J. Suzuki, M. Naruse, P. J. de Visser, P. P. van der Werf, T. M. Klapwijk, and J. J. A. Baselmans, Wideband on-chip terahertz spectrometer based on a superconducting filterbank, *J. Astron. Telesc. Instrum. Syst.* **5**, 035004 (2019).
- [4] B. Ho Eom, P. K. Day, H. G. LeDuc, J. Zmuidzinas, and A wideband, low-noise superconducting amplifier with high dynamic range, *Nat. Phys.* **8**, 623 (2012).
- [5] F. Arute *et al.*, Quantum supremacy using a programmable superconducting processor, *Nature* **574**, 505 (2019).
- [6] W. A. Phillips, Tunneling states in amorphous solids, *J. Low Temp. Phys.* **7**, 351 (1972).
- [7] C. Müller, J. H. Cole, and J. Lisenfeld, Towards understanding two-level-systems in amorphous solids: Insights from quantum circuits, *Rep. Prog. Phys.* **82**, 124501 (2019).
- [8] S. Hailey-Dunsheath *et al.*, Optical measurements of Super-Spec: A millimeter-wave on-chip spectrometer, *J. Low Temp. Phys.* **176**, 841 (2014).
- [9] D. Valenzuela, F. P. Mena, and J. Baselmans, in 30th International Symposium on Space THz Technology (Gothenburg, Sweden, 2019), p. 63.
- [10] W. Shan, Y. Sekimoto, and T. Noguchi, Parametric amplification in a superconducting microstrip transmission line, *IEEE Trans. Appl. Supercond.* **26**, 1 (2016).
- [11] J. M. Martinis, K. B. Cooper, R. McDermott, M. Steffen, M. Ansmann, K. D. Osborn, K. Cicak, S. Oh, D. P. Pappas, R. W. Simmonds, and C. C. Yu, Decoherence in Josephson Qubits from Dielectric Loss, *Phys. Rev. Lett.* **95**, 210503 (2005).
- [12] B. A. Mazin, D. Sank, S. McHugh, E. A. Lucero, A. Merrill, J. Gao, D. Pappas, D. Moore, and J. Zmuidzinas, Thin film dielectric microstrip kinetic inductance detectors, *Appl. Phys. Lett.* **96**, 102504 (2010).
- [13] S. Beldi, F. Boussaha, J. Hu, A. Monfardini, A. Traini, F. Levy-Bertrand, C. Chaumont, M. Gonzales, J. Firminy, F. Reix, M. Rosticher, S. Mignot, M. Piat, and P. Bonifacio, High Q-factor near infrared and visible Al_2O_3 -based

- parallel-plate capacitor kinetic inductance detectors, *Opt. Express* **27**, 13319 (2019).
- [14] S. Hahnle, N. v. Marrewijk, A. Endo, K. Karatsu, D. J. Thoen, V. Murugesan, and J. J. A. Baselmans, Suppression of radiation loss in high kinetic inductance superconducting co-planar waveguides, *Appl. Phys. Lett.* **116**, 182601 (2020).
- [15] A. D. O'Connell, M. Ansmann, R. C. Bialczak, M. Hofheinz, N. Katz, E. Lucero, C. McKenney, M. Neeley, H. Wang, E. M. Weig, A. N. Cleland, and J. M. Martinis, Microwave dielectric loss at single photon energies and millikelvin temperatures, *Appl. Phys. Lett.* **92**, 112903 (2008).
- [16] S. Hahnle, K. Kouwenhoven, B. Buijtendorp, A. Endo, K. Karatsu, D. J. Thoen, V. Murugesan, and J. J. A. Baselmans, Superconducting Microstrip Losses at Microwave and Sub-millimeter Wavelengths, *Phys. Rev. Appl.* **16**, 014019 (2021).
- [17] B. T. Buijtendorp, J. Bueno, D. J. Thoen, V. Murugesan, P. M. Sberna, J. J. A. Baselmans, S. Vollebregt, and A. Endo, Characterization of low-loss hydrogenated amorphous silicon films for superconducting resonators, *J. Astron. Telesc. Instrum. Syst.* **8**, 028006 (2022).
- [18] J. Gao, A. Vayonakis, O. Noroozian, J. Zmuidzinas, P. K. Day, and H. G. Leduc, Measurement of loss in superconducting microstrip at millimeter-wave frequencies, *AIP Conf. Proc.* **1185**, 164 (2009).
- [19] A. Endo, C. Sfiligoj, S. J. C. Yates, J. J. A. Baselmans, D. J. Thoen, S. M. H. Javadzadeh, P. P. van der Werf, A. M. Baryshev, and T. M. Klapwijk, On-chip filter bank spectroscopy at 600–700 GHz using NbTiN superconducting resonators, *Appl. Phys. Lett.* **103**, 032601 (2013).
- [20] J. Gao, Ph.D. thesis, California Institute of Technology, 2008.
- [21] M. Molina-Ruiz, Y. J. Rosen, H. C. Jacks, M. R. Abernathy, T. H. Metcalf, X. Liu, J. L. DuBois, and F. Hellman, Origin of mechanical and dielectric losses from two-level systems in amorphous silicon, *Phys. Rev. Mater.* **5**, 035601 (2021).
- [22] P. Sarro, C. de Boer, E. Korkmaz, and J. Laros, Low-stress PECVD SiC thin films for IC-compatible microstructures, *Sens. Actuator A Phys.* **67**, 175 (1998).
- [23] D. Brassard and M. A. El Khakani, Dielectric properties of amorphous hydrogenated silicon carbide thin films grown by plasma-enhanced chemical vapor deposition, *J. Appl. Phys.* **93**, 4066 (2003).
- [24] Y. Mishima and T. Yagishita, Investigation of the bubble formation mechanism in a-Si:H films by Fourier-transform infrared microspectroscopy, *J. Appl. Phys.* **64**, 3972 (1988).
- [25] J. Wang, L. Wu, X. Chen, W. Zhuo, and G. Wang, Avoiding blister defects in low-stress hydrogenated amorphous silicon films for MEMS sensors, *Sens. Actuator A Phys.* **276**, 11 (2018).
- [26] P. J. de Visser, S. A. H. de Rooij, V. Murugesan, D. J. Thoen, and J. J. A. Baselmans, Phonon-Trapping-Enhanced Energy Resolution in Superconducting Single-Photon Detectors, *Phys. Rev. Appl.* **16**, 034051 (2021).
- [27] D. J. Thoen, B. G. C. Bos, E. A. F. Haalebos, T. M. Klapwijk, J. J. A. Baselmans, and A. Endo, Superconducting NbTiN thin films with highly uniform properties over a \varnothing 100 mm wafer, *IEEE Trans. Appl. Supercond.* **27**, 1 (2017).
- [28] E. P. van de Ven, Advances in plasma enhanced thin film deposition, *Proc. SPIE, Monitoring and Control of Plasma-Enhanced Processing of Semiconductors* **1037**, 117 (1989).
- [29] R. M. J. Janssen, J. J. A. Baselmans, A. Endo, L. Ferrari, S. J. C. Yates, A. M. Baryshev, and T. M. Klapwijk, High optical efficiency and photon noise limited sensitivity of microwave kinetic inductance detectors using phase readout, *Appl. Phys. Lett.* **103**, 203503 (2013).
- [30] J. van Rantwijk, M. Grim, D. van Loon, S. Yates, A. Baryshev, and J. Baselmans, Multiplexed readout for 1000-pixel arrays of microwave kinetic inductance detectors, *IEEE Trans. Microwave Theory Techn.* **64**, 1876 (2016).
- [31] P. K. Day, H. G. LeDuc, B. A. Mazin, A. Vayonakis, and J. Zmuidzinas, A broadband superconducting detector suitable for use in large arrays, *Nature* **425**, 817 (2003).
- [32] The measured Fabry-Perot peaks differ in intensity, corresponding to different mm-submm powers being received by the MKIDs. We observe that the measured Q factors are independent of the powers received by the MKIDs, indicating that the MKIDs' responses are linear within the range of powers in which we perform our measurements.
- [33] M. Pollnau and M. Eichhorn, Spectral coherence, part I: Passive-resonator linewidth, fundamental laser linewidth, and Schawlow-Townes approximation, *Prog. Quantum Electron.* **72**, 100255 (2020).
- [34] Sonnet User's Guide — Sonnet 17, <http://www.sonnet-software.com/support/manuals.asp>.
- [35] See Supplemental Material at <http://link.aps.org/supplemental/10.1103/PhysRevApplied.18.064003> for details about the calculation of the correlation between the internal mm-submm powers and the internal quality factors of the Fabry-Perot resonators.
- [36] M. S. Khalil, M. J. A. Stoutimore, F. C. Wellstood, and K. D. Osborn, An analysis method for asymmetric resonator transmission applied to superconducting devices, *J. Appl. Phys.* **111**, 054510 (2012).
- [37] L. Faoro and L. B. Ioffe, Interacting tunneling model for two-level systems in amorphous materials and its predictions for their dephasing and noise in superconducting microresonators, *Phys. Rev. B* **91**, 014201 (2015).
- [38] G. Cataldo, J. A. Beall, H.-M. Cho, B. McAndrew, M. D. Niemack, and E. J. Wollack, Infrared dielectric properties of low-stress silicon nitride, *Opt. Lett.* **37**, 4200 (2012).
- [39] G. Cataldo, E. J. Wollack, A. D. Brown, and K. H. Miller, Infrared dielectric properties of low-stress silicon oxide, *Opt. Lett.* **41**, 1364 (2016).